A Scalable CMOS Molecular Electronics Chip for Single-Molecule Biosensing

Drew A. Hall, *Senior Member, IEEE*, Nagaraj Ananthapadmanabhan, Chulmin Choi, Le Zheng, *Member, IEEE*, Paul P. Pan, Christoph Von Jutrzenka, Thuan Nguyen, Jose Rizo, Macklan Weinstein, Raymond Lobaton, Prem Sinha, Trevor Sauerbrey, Cruz Sigala, Kathryne Bailey, Paul J. Mudondo, Ashesh Ray Chaudhuri, Simone Severi, Carl W. Fuller, James M. Tour, Sungho Jin, Paul W. Mola, and Barry Merriman

***Abstract*—This work reports the first CMOS molecular electronics chip. It is configured as a biosensor, where the primary sensing element is a single molecule "molecular wire" consisting of a ∼100 GΩ, 25 nm long alpha-helical peptide integrated into a current monitoring circuit. The engineered peptide contains a central conjugation site for attachment of various probe molecules, such as DNA, proteins, enzymes, or antibodies, which program the biosensor to detect interactions with a specific target molecule. The current through the molecular wire under a dc applied voltage is monitored with millisecond temporal resolution. The detected signals are millisecond-scale, picoampere current pulses generated by each transient probe-target molecular interaction. Implemented in a 0.18 μm CMOS technology, 16k sensors are arrayed with a 20 μm pitch and read out at a 1 kHz frame rate. The resulting biosensor chip provides direct, real-time observation of the single-molecule interaction kinetics, unlike classical biosensors that measure ensemble averages of such events. This molecular electronics chip provides a platform for putting molecular biosensing "on-chip" to bring the power of semiconductor chips to diverse applications in biological research, diagnostics, sequencing, proteomics, drug discovery, and environmental monitoring.**

***Index Terms*—Single-molecule biosensor, molecular electronics, transimpedance amplifier, high-impedance sensor, biosensor.**

I. Introduction

MOLECULAR electronics is the concept of using single molecules as functional circuit elements. This concept was first put forth in the 1974 work of Aviram and Ratner [1], which envisioned special molecules to be used as rectifiers or switches. At the time, integrated circuits were rapidly shrinking following Moore's Law [2], and their work was motivated, in part, by considerations about the ultimate physical limits of circuit miniaturization. It was also inspired by then-recent discoveries from the 1960s that a single biomolecule, such as a cytochrome protein, could carry out complex electron transfer processes [3]. This was not long after Feynman's seminal 1959 proposal to extend engineering to the molecular scale [4]. While Feynman had, in effect, imagined nanotechnology as molecular mechanical engineering, the work of Aviram extended this to encompass molecular electrical engineering.

The visionary work of Aviram remained entirely theoretical for decades due to the inability to manipulate single molecules. This changed in 1998 when Tour and Reed [5] experimentally produced the first molecular electronic circuit by measuring the resistance of a single benzene molecule suspended between gold nanoelectrodes. At that time, the demonstration of the first molecular circuit was hailed as the scientific "Breakthrough of the Year" in Science [6], but the accompanying editorial noted that the real impact would come when molecular circuit elements could be integrated into CMOS chips.

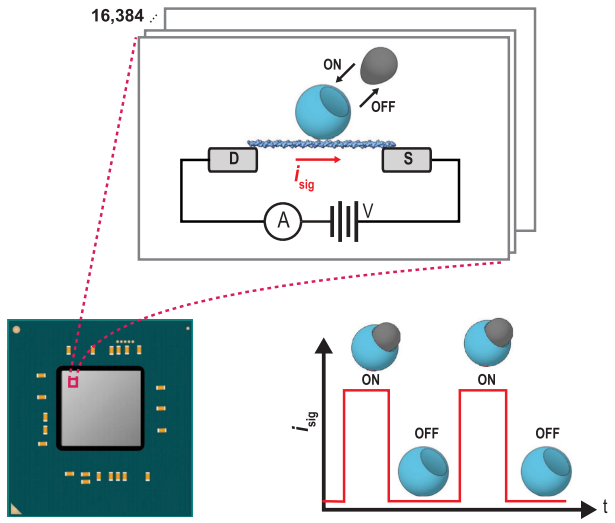

Fig. 1. Overview of a highly multiplexed, scalable CMOS-based molecular biosensor for single-molecule sensors.

Manuscript received 16 July 2022; revised 2 September 2022; accepted 25 September 2022. Date of publication 3 October 2022; date of current version 14 February 2023. This work was supported in part by the Office of the Director of National Intelligence (ODNI) and in part by Intelligence Advanced Research Projects Activity (IARPA) under Contract 2019-19081900003. This paper was recommended by Associate Editor P. Mohseni. *(Corresponding authors: Drew A. Hall; Barry Merriman.)*

Drew A. Hall is with the Department of Electrical and Computer Engineering, University of California, San Diego, CA 92093 USA (e-mail: drewhall@ucsd.edu).

Nagaraj Ananthapadmanabhan, Chulmin Choi, Le Zheng, Paul P. Pan, Christoph Von Jutrzenka, Thuan Nguyen, Jose Rizo, Macklan Weinstein, Raymond Lobaton, Prem Sinha, Trevor Sauerbrey, Cruz Sigala, Kathryne Bailey, Paul J. Mudondo, Carl W. Fuller, Sungho Jin, Paul W. Mola, and Barry Merriman are with the Roswell Biotechnologies, San Diego, CA 92121 USA (e-mail: barry.merriman@roswellbiotech.com).

Ashesh Ray Chaudhuri and Simone Severi are with imec, 3001 Heverlee, Belgium.

James M. Tour is with Rice University, Houston, TX 77005 USA.

Color versions of one or more figures in this article are available at https://doi.org/10.1109/TBCAS.2022.3211420.

Digital Object Identifier 10.1109/TBCAS.2022.3211420

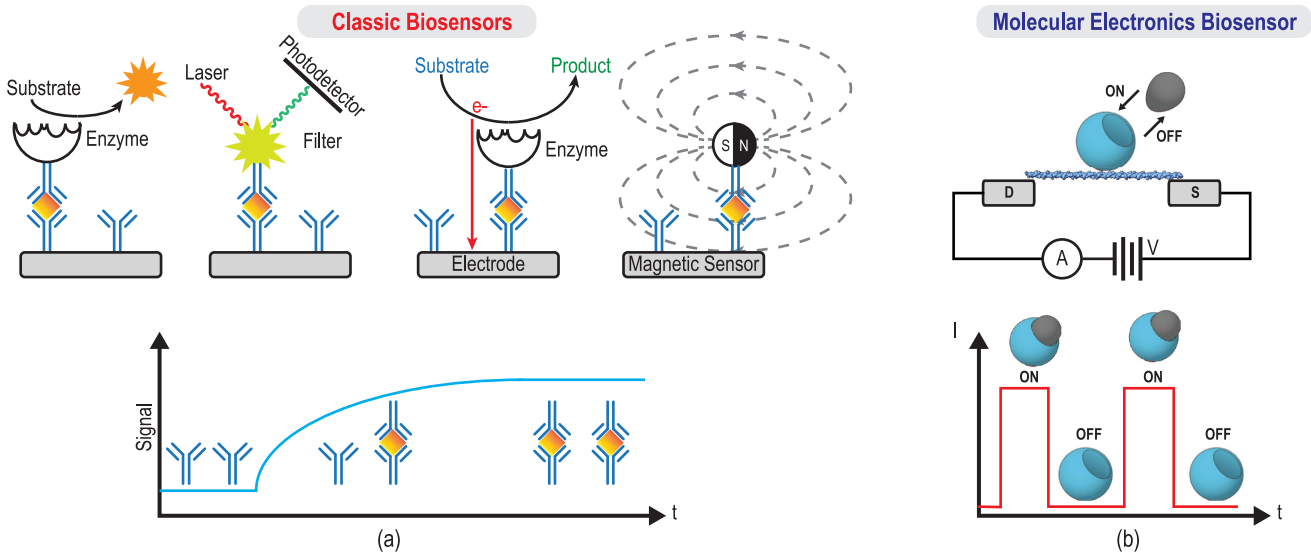

Fig. 2. (a) Overview of classical biosensors; (b) Molecular electronic single-molecule biosensor.

In the present work, we introduce such a molecular electronics CMOS chip (see Fig. 1), realizing this nearly 50-year-long quest for molecular electronics – with the notable distinction that, instead of molecules being used as logic elements or memory bits, as envisioned by the pioneers of the field, we propose that using single molecules as sensor elements is the "killer application" for molecular electronics. This is because silicon is exceptionally well-suited for logic and memory devices, as evidenced by nearly 60 years of Moore's Law scaling [7], [8], [9], while silicon has limited intrinsic sensing abilities, especially for biosensing [10], [11]. The primary motivation for a molecular electronics solution to sensing is to fundamentally solve the well-known "More-Than-Moore" scaling problem for sensors, which is that transducer scaling is commonly the limiter to scaling chip-based sensor devices. Thus, the ideal solution is to have the transducer be a single molecule, which is already shrunk to the physical limit and will never inhibit future circuit scaling.

As shown in Fig. 1, the sensing element is a 25 nm molecular wire connected to metal nanoelectrodes, which feed into a current monitoring circuit. The molecular wire contains a central conjugation site for attachment of various probe molecules (*e.g.,* DNA, proteins, enzymes, or antibodies) and is flanked by metal-binding domains for selective coupling to the nanoelectrodes. These current monitoring pixels are arranged in a 16k sensor array that provides control of the array and digital data readout at a 1 kHz frame rate. The molecular wires (and conjugated probes) are actively loaded into the circuit at startup using dielectrophoresis to trap molecules in the nanoelectrodes. Then, the current through the bridge molecule under a dc applied voltage is monitored with millisecond temporal resolution. The detected signals are millisecond-scale current pulses generated by each transient probe-target molecular interaction. This provides direct, real-time detection of the single-molecule interaction kinetics, in contrast to classical biosensors that often rely on indirect reporter mechanisms and measure ensemble averages of such events across many molecules and long times. This paper extends the work presented in [12], [13].

The remainder of this paper is organized as follows: Section II explains the sensor concept and contrasts single-molecule sensors with classical biosensors. Section III describes the chip architecture, and Section IV details the circuit implementation. Sensor post-processing is covered in Section V, and Section VI reports electrical and *in-vitro* measurement results. Finally, concluding remarks are made in Section VII.

II. Single-Molecule Biosensing

A common problem in biosensing is to detect a specific target biomolecule in a sample and, most ideally, to provide a quantitative measure of the target molecule concentration. Physical methods such as mass spectrometry, infrared spectrometry, and other forms of spectroscopy identify target molecules based on their physical properties, such as charge, mass, or interactions with photons [14], [15], [16]. However, these approaches typically cannot easily identify specific, complex biomolecules such as proteins, DNA segments, and diverse biochemicals, particularly in complex backgrounds of other such molecules, as is common for un-purified biological samples [17].

Such target biomolecules in complex backgrounds are instead resolved by relying on a specific binding probe molecule that selectively and specifically binds to the target molecule [18]. Common binding pairs that can form a probe and target include single-stranded DNA (ssDNA) and its complementary strand, a receptor protein and a ligand (*e.g.*, antibody-antigen pair), or a synthetic DNA aptamer and its target molecule. Given a specific binding pair, such as an antibody-antigen, in a classical biosensor concept, such as those shown in Fig. 2(a), many probe molecules are attached to a solid support. When exposed to a sample, some target molecules present in the sample are bound and detected either through the presence of a reporter label (such as a fluorescent dye attached to the target) or a reporter mechanism that indirectly produces a localized detectable label (such as a secondary antibody with a dye label or linked to an enzyme that catalyzes an observable reaction, as in ELISA). Many such "labeled" biosensing schemes have

been reported with optical [19], enzymatic [20], electrochemical [21], [22], [23], [24], [25], [26], [27], and magnetic [28], [29], [30] reporters, among others. Label-free approaches have also been developed where the binding event changes a measurable physical property of the surface, such as the reflectance, plasmon resonance, or charge [31], [32], [33], [34]. The temporal trajectory of such a reaction, if it were observed, would typically be a curve that picks up rapidly after the introduction of the analyte and saturates at some endpoint, as indicated in Fig. 2(a), representing the bulk, equilibrium statistical mechanics of the binding interaction and reporter mechanism. In practice, the measurement is often performed at the endpoint, such as reading out the final equilibrium amount of fluorescence from a reporter dye.

In contrast to these classical biosensors, the single-molecule binding sensor reported here, see Fig. 2(b), measures the current passing through the molecular wire under an applied dc voltage. In this system, the individual molecular probe-target binding events change the impedance of the complex. These bio-molecular binding events are commonly reversible, hence, the actual bound state only exists *transiently* for some stochastic dwell time, and the probe will dynamically bind and unbind with target molecules in solution. As shown in Fig. 2(b), the ideal readout is a series of current pulses, each representing the direct observation of a single-molecule binding event. The duration of any given binding event is a random variable, sampled from the Boltzmann Distribution of statistical mechanics, which in turn depends on the binding energy and temperature. The waiting time between binding events is also a random variable, ideally exponentially distributed, where the mean waiting time is inversely related to the target molecule concentration. Thus, the mean waiting time provides a quantitative measure of the target concentration. One convenient expression for such a measure is the total fraction of time the sensor is in the bound state, which ideally obeys a classical first-order Michaelis-Menten rate law as a function of the target concentration [35].

Early scientific studies of electronic detection of single-molecule binding were done by non-specifically attaching single probe molecules on long carbon nanotubes and monitoring the nanotube current [36], [37], [38]. For the class of biosensors presented here to be both high performance and commercially viable, the design goal for the molecular component is precision at the nanoscale and manufacturability – that is, to have precision-engineered molecular constructs with precisely defined probe conjugation sites and end groups for nanoelectrode attachment, and that can be mass-produced by existing industrial means. Suitable molecular wires that fit these constraints include protein alpha-helical peptides and double-stranded DNA (dsDNA). The present work uses the peptide format as they have higher conductivity and are easier to synthesize with attachment points. The conductivity of peptide molecular wires and other proteins has recently been studied using sophisticated scanning probe techniques to directly measure the current passing through single protein molecules [39], [40], [41], [42]. These molecular wires (or "bridge" molecules) have much lower conductivity than the carbon nanotubes; here, the nominal resistance is $\sim$100 GΩ for the 25 nm alpha-helical peptide. These molecules may not have a net charge but are polarizable and thus can be

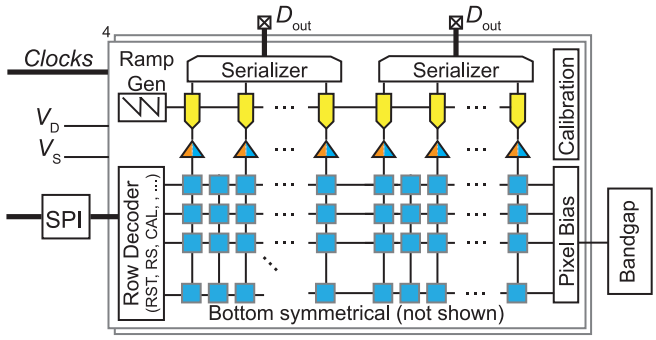

Fig. 3. System architecture.

electrically attracted to the nanoelectrodes by applying an ac voltage, a process known as dielectrophoresis (DEP) [43]. This active mechanism is used to rapidly load the molecules into the nanoelectrodes.

The signal generation mechanism in these sensors has not been fully characterized and remains largely an empirical observation. Multiple possible candidate modes for generating current modulation are evident, including field effects (from charges in the probe region modulating electron transport through the molecular wire), redox reactions, reconfigurations of the ion cloud around the molecules, and changes in the physical conduction paths available to charge transport electrons due to probe-target interactions. For example, in the special case of carbon nanotube sensors, an explicit field effect mechanism has been demonstrated to be the dominant signal generation mode [38], [44]. In part, this was demonstrated by increasing solution salt levels (decreasing the Debye shielding length) [44], which decreases the signal to near zero. Doing similar Debye shielding experiments for our sensors results in approximately 70% of the signal being eliminated at high salt, suggesting that field effects are a major component, but not the sole component, of the signal generation mechanism.

III. System Architecture

To understand the initial system requirements, small nanoelectrode test arrays were fabricated on a silicon substrate. These discrete sensor devices were read out using a custom-designed front-end built using off-the-shelf components with support for up to 8 sensors. This system allowed rapid design exploration, such as trying different sensor geometries, electrode materials, applied bias voltage, and bridge molecules. After significant experimentation using this system, we found that for peptide-based bridges, the current ranged from 0.1 to 100 pA with a 0.5 V bias and a 1 kSps sampling rate was sufficient to capture most interaction events of interest. These specifications were then used to architect a scalable, high-density CMOS front-end with integrated sensors.

As shown in Fig. 3, this chip is arranged like a CMOS image sensor with a 2D pixel matrix divided into 4 sub-arrays, each containing 4096 (64×64) pixels for a total array of 16384 pixels. This number of pixels supports redundancy, multiplexing, and reduction of assay response time. Each pixel contains a transimpedance amplifier, a column driver, and an electrode

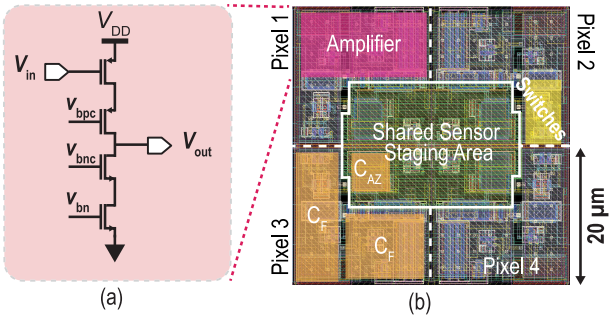

Fig. 4. (a) Schematic of the pixel amplifier and (b) Annotated layout of a 2×2 grid of pixels.

pair exposed to the solution for the bridge molecule to attach. The pixel area is limited to 20×20 μm^2, a constraint driven by the desire to have a full reticle chip with 1.5 million sensors for future high-throughput applications in DNA sequencing and proteomics. Each pixel must consume less than 2.5 μW to keep the surface heating less than 5 °C inside the flow cell with static fluid at the million-pixel scale. The top two rows of each sub-array are "dark" pixels, where the electrodes are covered with oxide and thus not exposed to the solution, which serve as negative controls.

The sensor array is typically operated in a rolling shutter mode (*i.e.*, rows are sequentially reset with staggered read times). The reset can also be overridden through a global reset. A shift-register-based row decoder supplies the pixel control signals (*e.g.*, reset, mode, calibration, gain, etc.) and chooses a row of sensors to be read out. The shift register-based decoder avoids spurious glitches from a traditional decoder and allows for an arbitrary number of rows, whereas a decoder is limited to a power of 2. These digital signals are re-buffered between each sub-array by repeater cells. The selected row of pixels is read out by column-parallel ADCs butterflied along the top and bottom of the array. The top ADCs read pixels in the odd columns of the array, whereas pixels in even columns are read by the bottom ADCs. This split strategy allows the ADC to have twice the pixel pitch (*i.e.*, 40 μm). All other circuits (*e.g.*, row decoder unit cell, ADC, pixel bias, repeaters, etc.) are pitch-matched to the pixel (20 μm) to facilitate assembly. The ADC outputs are aggregated by serializers into 16 lanes and captured using an FPGA. The FPGA also provides all clock and control signals to the chip and configures the chip through a serial peripheral interface (SPI). The sensor bias voltages, $V_{\rm S}$ and $V_{\rm D}$, are provided from off-chip for maximum flexibility.

IV. Circuit Implementation

A. Auto-Zeroed Transimpedance Amplifier

The core of the pixel is a capacitive transimpedance amplifier (C-TIA) that integrates the pA-level sensor current on a feedback capacitor, $C_{\rm F}$. The amplifier is implemented with a single-ended, common-source amplifier, as shown in Fig. 4(a). The input device is a 3 V I/O PMOS transistor for lower flicker (1/*f*) noise and cascoded with core devices for high output impedance. The pixel supply voltage is 2.1 V, allowing for a high output swing.

The amplifier was sized to have a dc gain of 70 dB and a 7 MHz open-loop unity-gain bandwidth with a 1 μA bias current. Due to the limited area (400 μm^2), it was impossible to size the transistors large enough to have a low flicker (1/*f*) noise corner. Instead, this was mitigated actively through auto-zeroing, which also samples the correct bias voltage. With the post-processing scheme described later, most of the top metal is needed for the sensor staging area. Unfortunately, in this process, the top metal is required to contact the metal-insulator-metal (MIM) capacitors. Thus, the feedback capacitors were implemented using all the available MIM area since they need to be very linear, and the auto-zero capacitor, $C_{\rm AZ}$, was implemented using a MOSFET capacitor underneath the staging area, as shown in Fig. 4(b). To create a larger window for post-processing, the pixels are arranged in a 2×2 grid with mirroring and flipping to group the sensor openings. This larger window is needed during the sacrificial etch process described later. Single vias to the top metal will eventually be coupled to the nanoelectrodes; they are all shorted together during fabrication by the top metal covering the staging area. This also provides ESD protection from the source-side connection.

Ideally, one would route currents to the pixels and locally generate the necessary bias voltages to minimize coupling and the effect of mismatch, but there is insufficient remaining area at the desired pixel pitch. Instead, the bias generation is shared by all pixels in a row. Row level (vs. column or another arrangement) was chosen since the pixels are all reset simultaneously, thus correlating the bias disturbance. An on-chip bandgap reference generates a supply- and temperature-insensitive current that is then mirrored to 256× replica bias circuits (one per row per sub-array). The repeater cells that buffer the digital signals also incorporate decoupling capacitors for the analog bias signals.

The pixel operation, shown in Fig. 5, is as follows: 1) During reset (RST), the capacitance at the virtual ground node is charged to $V_{\rm D}$. A bias voltage, $V_{\rm S}$, is constantly applied to the other side of the sensor. The amplifier is auto-zeroed at this time to remove its 1/*f* noise and set the bias by sampling these on $C_{\rm AZ}$ = 75 fF. 2) During the integration phase, the sensor current is integrated on a 1-bit selectable feedback capacitor, $C_{\rm F}$ = 200 fF (150 pA dynamic range) or 400 fF (300 pA dynamic range). Normal operation ping-pongs between reset (15.625 μs) and integration (984.375 μs). At startup, a switch (MODE) removes the sensor from the circuit, and a calibration current is applied to verify the pixel functionality. The calibration current is supplied from off-chip, attenuated, and copied to each column using a cascoded current mirror. All switches connected to the sensitive virtual ground node are low-leakage T-switches [22], where the internal switch node is driven to $V_{\rm D}$ to minimize the voltage drop across the switch in the off-state.

B. Split Buffer Column Driver

The C-TIA drives a split buffer, half of which is inside the pixel, with the rest shared by all pixels in the column, as shown in Fig. 6. This architecture was chosen over a conventional source follower-based column driver because it has higher linearity and is inherently a current-mode circuit with low impedance nodes

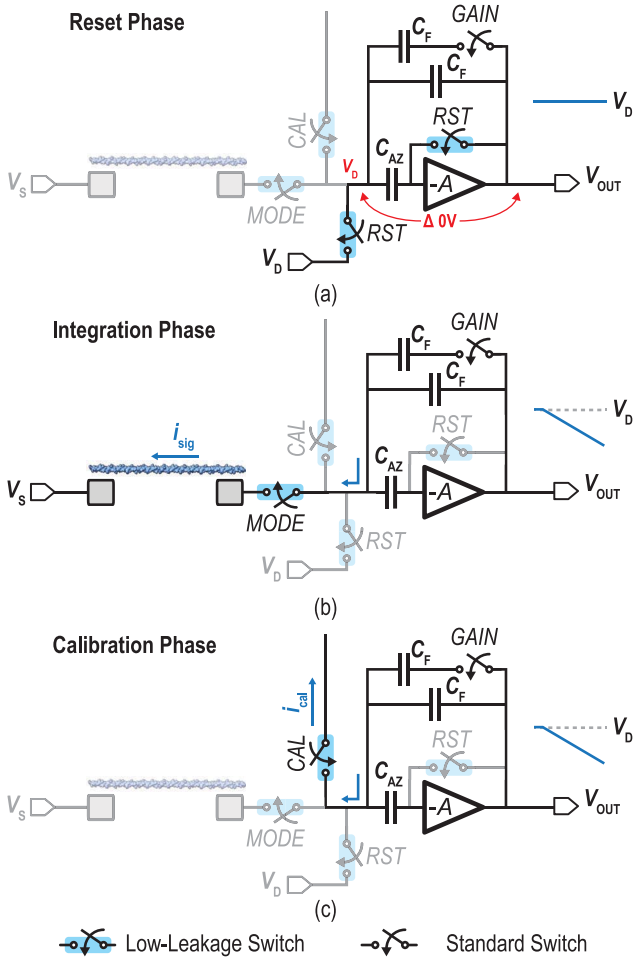

Fig. 5. Schematic of auto-zeroed transimpedance amplifier during the (a) Reset, (b) Integration, and (c) Calibration phases.

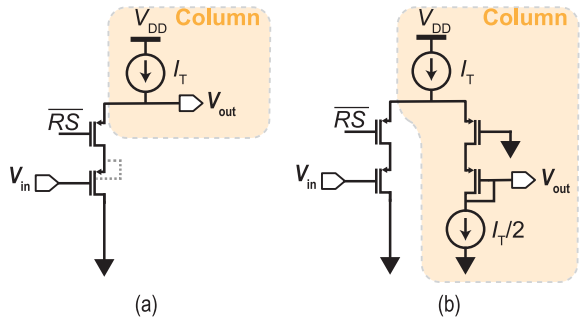

Fig. 6. Schematics of a (a) Conventional source follower with optional body tie and (b) Split buffer amplifier.

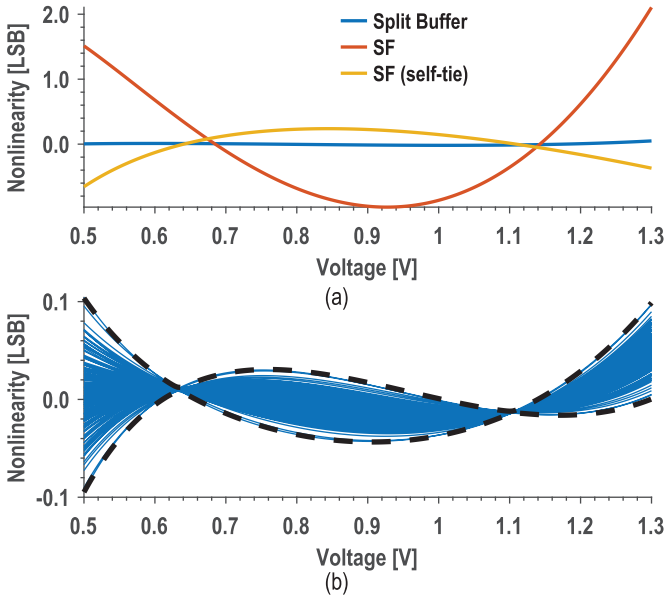

Fig. 7. Split buffer simulations showing (a) Nonlinearity and (b) Monte Carlo variation ($n = 100$).

for fast settling when switching rows. Even when the bulk of the source follower is tied to the source, the simulated source follower-based buffer nonlinearity is worse than the split buffer, as shown in Fig. 7(a). The split buffer does not need the body-source tie, simplifying the layout since all the PMOS devices can share a common n-well. The better linearity stems from the partial cancellation of nonlinearities due to the differential nature of the circuit. A Monte Carlo simulation with 100 runs was performed to demonstrate the circuit's robustness. As shown in Fig. 7(b), the worst-case nonlinearity is less than 0.2 LSBs across the entire voltage range.

With a 1000 frame/s sampling rate, the ADC has 15.625 μs for settling (2.825 μs) and conversion (12.8 μs). In both column driver approaches, there is a significant capacitance hanging on the output node consisting of the routing and the column drivers of all the off rows. This capacitance is 660 fF based on post-layout extraction. The buffer was designed to settle in less than 1.25 μs. Another benefit of the split buffer structure is that it allows for level-shifting such that the ADCs can operate from a nominal 1.8 V supply voltage.

C. Column-Parallel Single-Slope ADC

The 64 kSps ADCs are implemented using a single-slope architecture with two preamplifiers, a strong-arm latch, and an 11-bit counter, as shown in Fig. 8(a). The counter has an additional bit (not read out) to catch overflow without wrapping. Two preamps were used to suppress the latch's offset and minimize comparator kickback on the shared ramp signal. Each open-loop preamplifier consumes 28 μW and has a 100 MHz unity-gain bandwidth with 20 dB dc gain. The simulated input-referred noise of the amplifier is 74 μV_{rms}. Like the pixel, the preamplifier bias network is shared by all ADCs in a sub-array.

The shared ramp generator (one per side of each sub-array) is realized by an integrator with a programmable current source, as shown in Fig. 8(b). This amplifier-based feedback structure maintains the voltage across the current source (to maximize the linearity) while also providing a low output impedance to drive the preamplifiers. The ADC is reconfigurable between 8- and 10-bit modes by changing the clock. The integration current is digitally programmable via the SPI bus in 30 nA steps with a nominal 5 μA current. The current is integrated on a 12.8 pF

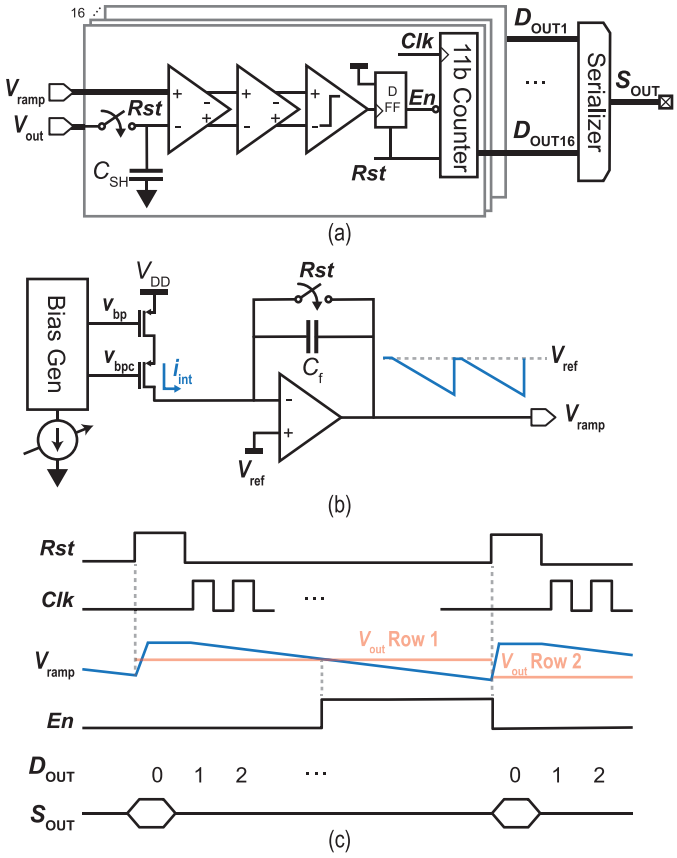

Fig. 8. Schematics of the (a) Column-parallel single-slope ADC and (b) Ramp generator; (c) Timing diagram.

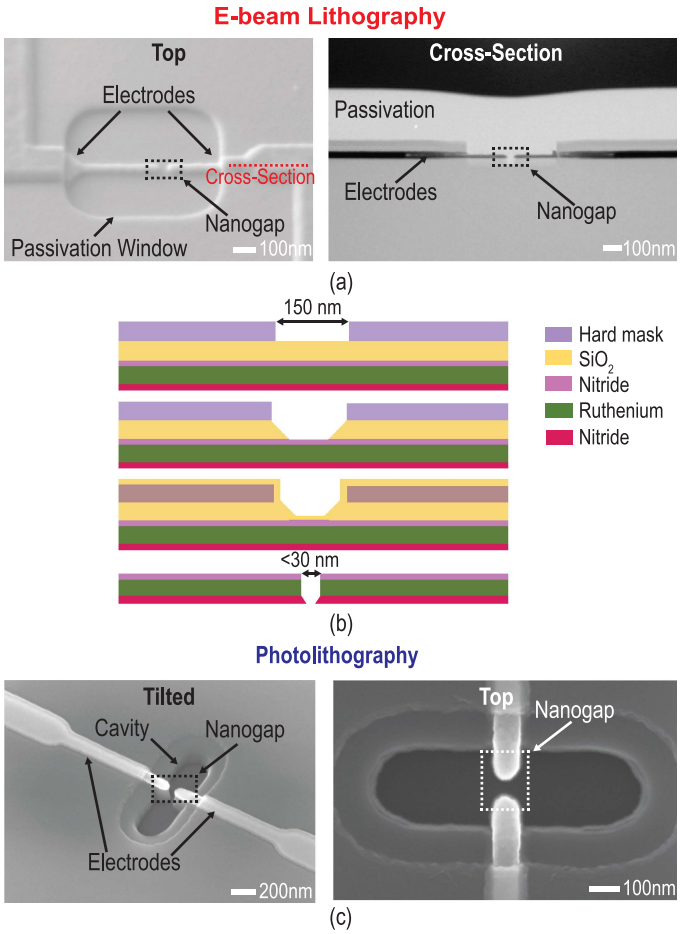

Fig. 9. (a) SEM images of nanoelectrodes fabricated via E-Beam lithothography. (b) Photolithography gap narrowing process and (c) SEM images of fabricated nanoelectrodes.

MIM capacitor. The amplifier is implemented with a single-stage folded-cascode structure with a dc gain of 84 dB and a 35 MHz unity-gain bandwidth.

Fig. 8(c) shows a timing diagram for each conversion. First, the voltage from the split buffer is sampled onto a capacitor. Simultaneously, the ramp generator, sparkle latch, and counter are reset. The ADC clock is gated by the reset signal and held low. Once the reset signal is de-asserted, the ramp generator starts integrating the current ramping down from the full-scale voltage toward zero. The counter increments each ADC clock cycle until the ramp signal crosses the value stored on the sample and hold capacitor, C_{SH}, after which a sparkle latch (a D flip-flop) captures the comparator output to prevent retriggering, and the counter stops incrementing. The ADC outputs are aggregated by a shift register-based serializer running at 11 Mbps with 16 lanes and captured using an off-chip FPGA. The data is shifted off during the reset period to minimize coupling.

V. Post-Processing

The precision-engineered molecular wires, such as dsDNA or the present helical peptides, are by design at the nanometer scale (<30 nm), thus requiring the gap between the electrodes to be smaller than what is possible in standard CMOS back end of the line (BEOL) metallization. Furthermore, the electrodes must be electrochemically stable in ionic solutions, precluding the use of standard metals like copper and aluminum. After a detailed material compatibility study, ruthenium (Ru) was chosen due to its foundry compatibility, robustness, and electrochemical performance. Two approaches were developed to pattern the nanoelectrodes, electron-beam lithography (EBL) (ideal for agile R&D) and conventional photolithography (ideal for mass production at CMOS foundries).

A. Electron-Beam Lithography

For EBL nanoelectrodes, the wafer is spin-coated with photoresist (NR9-6000PY) and patterned to selectively etch the sacrificial 23 × 15 μm^2 "bond pads" over the sensor vias using Aluminum Etchant Type A (Transene). This process leaves the outer real bond pads intact while exposing the tungsten vias in the common staging area for the electrodes of 4 adjacent pixels. This sacrificial approach is necessary as the top metal is too rough to pattern nanoelectrodes directly. The metal 5-6 vias are the last planarized layer in the commercial foundry's fabrication process ensuring planarity. Next, the nanoelectrodes are written by spin coating polymethyl methacrylate (PMMA) A2 and patterning it using a Vistec EBPG 5200 (4 nm beam radius, 30 keV accelerating voltage, and 10 pA beam current).

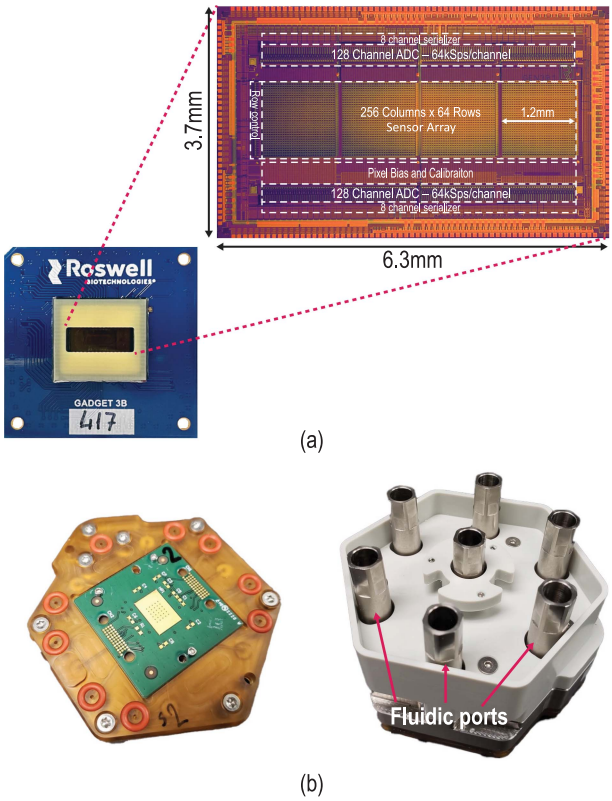

Fig. 10. (a) Annotated die micrograph on a "chip-on-board" package and (b) Photograph of the backside of packaged chip (left) and assembled re-usable version of the flowcell (right).

This results in 50 nm wide electrodes with less than 20 nm gaps. A 5 nm chromium (Cr) and 20 nm Ru film stack is deposited and subsequently lifted off. A second EBL process places a 5 nm Cr, 50 nm Ru, and 50 nm hafnium oxide (HfO) film stack to cap the vias and cover part of the wire with oxide to minimize current leakage into the electrolyte. Fig. 9(a) shows a representative nanoelectrode visualized using a Zeiss Sigma 500 emission scanning electron microscope (SEM) and a cross-section of the nanoelectrode.

B. Photolithography

It is important to have a photolithography process for producing nanoelectrodes that is fully foundry compatible and capable of producing nanoelectrodes at scale. For photolithography, the wafers are pulled before passivation with individual top metal pads for each electrode (instead of the sacrificial bond pad used for EBL). Tungsten vias and oxide are subsequently added and planarized. A blanket 3 nm tantalum nitride (TaN), 15 nm Ru, and 3 nm titanium nitride (TiN) film stack is deposited, followed by a 50 nm SiO_2 layer deposited with plasma-enhanced chemical vapor deposition (PECVD). Direct patterning of the nanoelectrode gap is well beyond the native resolution of current 200 mm tool lines. Instead, a gap-narrowing technique is employed that leverages these tools to achieve the required feature size. A deep-ultraviolet (DUV) resist is coated on the SiO_2 layer. After light-field exposure using 193 nm immersion lithography, the resist is developed, and the unprotected oxide is removed via RIE etching. A hard mask is deposited on the remaining SiO_2 structure, and a dark-field exposure is used to print a 150 nm gap into the SiO_2. A proprietary etch chemistry results in a tapered etch profile and achieves a final distance of 50 nm between the bottoms of the SiO_2 mandrels. To further reduce the electrode gap size, spacer patterning is employed. Highly conformal SiO_2 is deposited via plasma-enhanced atomic layer deposition (PEALD) atop the SiO_2 mandrels, as shown in Fig. 9(b). The resulting $<$30 nm gap is transferred into the metal layers by ion-beam etching through the underlying SiO_2 matrix. To protect the vias from electrochemical reactions, 20 nm SiO_2 and 30 nm SiN are deposited by PECVD. Passivation over the bond pads is removed by a photolithographically enabled oxide etch landing on the bond pad layer. To open the nanoelectrode area, a DUV resist is spin-coated as an etch mask for a cavity (500×1100 nm^2). After exposure, the resist is developed, and the passivation dielectric layers are etched using IBE. Fig. 9(c) shows SEM images of the resulting nanoelectrodes.

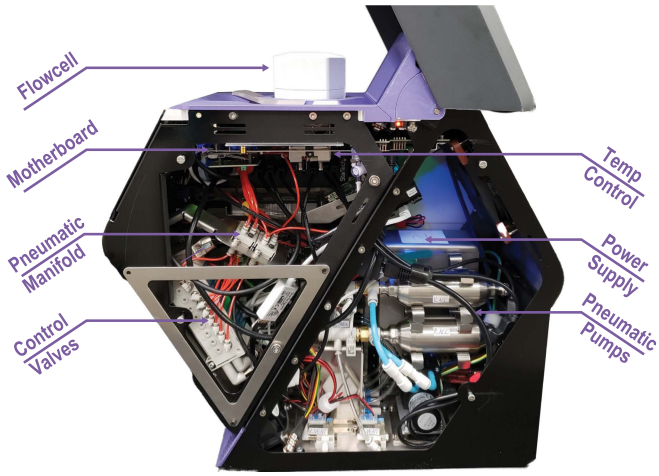

Fig. 11. Annotated photograph of instrument.

VI. Measurement Results

The reported chip was fabricated in a 180 nm CMOS process with a multilayer mask (MLM). Wafers were post-processed to fabricate nanoelectrodes with a range of gaps (10-12 nm, 14-16 nm, 17-20 nm, and 20-30 nm) using EBL and photolithography. The chips were wire-bonded directly to a printed circuit board (PCB) with partial encapsulation to expose the pixel array, as shown in Fig. 10(a), and mounted in a custom flow cell with a platinum rooftop pseudo-reference electrode and fluidic access ports [see Fig. 10(b)]. The pseudo-reference electrode sets the bulk solution potential and is driven by a low-impedance source rather than a potentiostat.

A. Instrument

The chip cartridge plugs into a dry instrument that controls reagent delivery and handles all electrical signals. Fig. 11 shows a photograph of the instrument containing the microfluidic flow cell, motherboard, temperature controller, power supply, and pneumatic control for reagent delivery. The motherboard has an FPGA (Opal Kelly XEM6310), an ac waveform generator

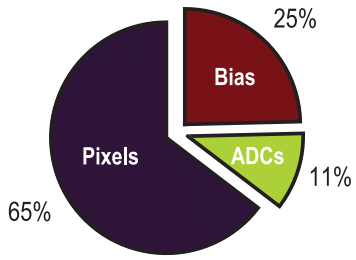

Fig. 12. Measured power consumption.

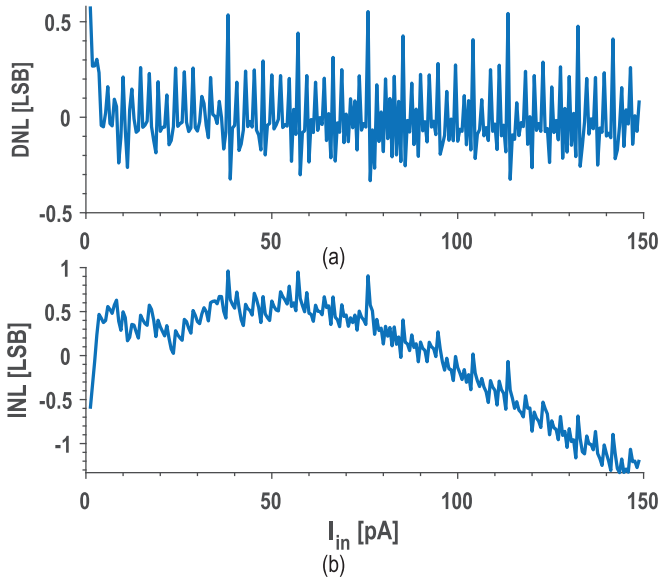

Fig. 13. Measured signal path (a) DNL and (b) INL.

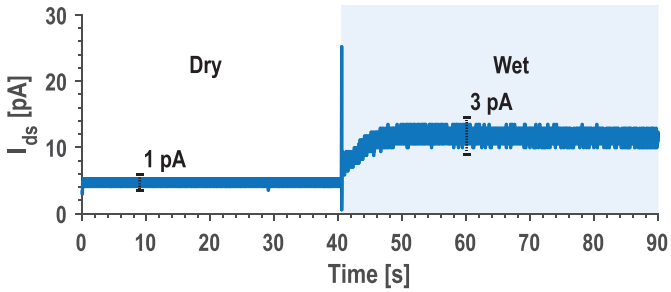

Fig. 14. Measured leakage (a) Dry and (b) Wet.

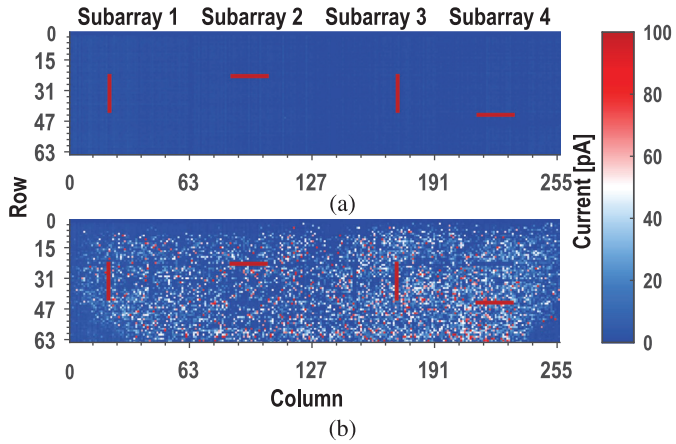

Fig. 15. Measured signal across array at the (a) Start of the experiment prior to loading the bridges and (b) After the assay completion.

for dielectrophoresis, and an SPI bus for monitoring the chip's critical currents, voltages, and temperatures. The FPGA acquires the ADC data (at 20 MB/s), buffers it, and sends it to a computer via USB, where it is streamed to a solid-state disk. The data is subsequently stored in HD5 files for downstream analysis. The sample being tested is loaded into the center well of the flowcell cartridge, whereas all other reagents are stored in the additional wells in the cartridge, and all are delivered to the chip through pneumatic control in a software-programmable sequence.

B. Electrical Characterization

The chip operates off a 2.1 V supply for the pixels and buffers and 1.8 V for the remaining circuits, consuming 58 mW, as shown in Fig. 12. Most of the power is dissipated in the pixels (37.8 mW) followed by the ADCs (14.4 mW). The measured input-referred integrated noise is 39 fA_{rms} for $C_F = 200$ fF and 76 fA_{rms} for $C_F = 400$ fF. Fig. 13 shows the measured signal path (pixel and ADC) linearity acquired by sweeping the calibration current across the input range. The average differential nonlinearity (DNL) is +1.5/-0.7 LSB, and the integrated nonlinearity (INL) is ±2 LSB. The measured residual input-referred offset is 2.5-5 pA across the array due to the buffer and ADC preamplifier offsets, which are not auto-zeroed. The measured leakage current fluctuates by <1 pA dry and 3 pA in distilled water, with minimal dependence on V_{DS} (nominally $V_D = 1.3$ V and $V_S = 0.8$ V), as shown in Fig. 14. The digital signal integrity was measured using a Keysight Infinium oscilloscope. When shifting the data off the chip at 80 MHz, the signal eye diagram had an opening of 9.7 ns and 1.3 V. Finally, Fig. 15 shows an illustrative example of the entire array being read out before and while an assay was run. The red lines in Fig. 15(a) are control pixels where the nanogap is intentionally shorted to debug sensor failures. Fig. 15(b) shows a snapshot of the array during an assay where the pixels' real-time activity is observed.

C. In-Vitro Characterization

The bridge molecules must be loaded into the circuit for use as a sensor. Delivery by passive diffusion alone can require over 24 hours, even at a high concentration. Instead, the much faster process of active dielectrophoretic trapping is employed by applying an ac voltage to the electrodes for 10-second intervals, as shown in Fig. 16. The "boot up" phase consists of up to 10 rounds of such active bridging, applying a 1.6 V_{pp} sinusoid at 100 kHz through V_S with V_D held at a fixed potential (by keeping the amplifier in reset). During the bridging phase, the buffer is a low ionic strength solution to prevent Debye screening. After each DEP round, the array is read out to determine if a bridge was incorporated, as observed by an increase in the pixel current. A pixel is marked as bridged if two successive measurements show an elevated current, and trapping is stopped to prevent additional bridging. An exemplar SEM image of a single "dumbbell" bridge (made observable by the addition of two 10 nm diameter gold

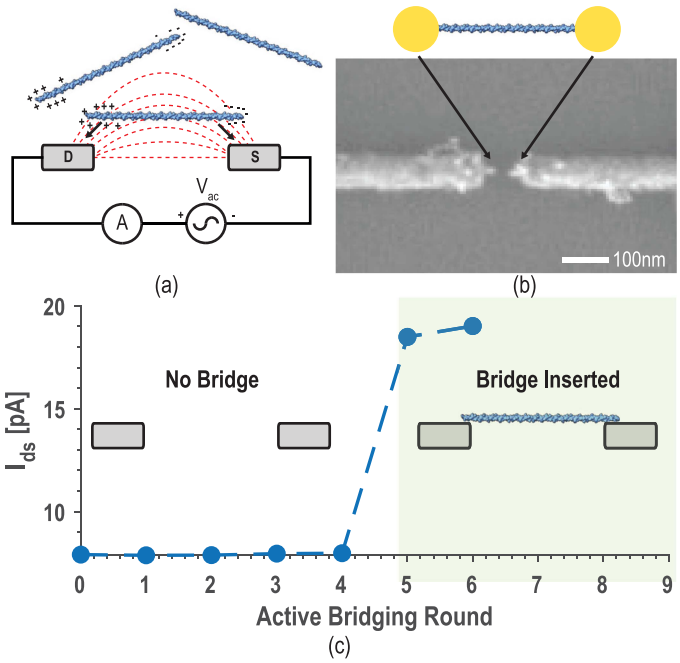

Fig. 16. (a) Dielectrophoretic trapping concept, (b) SEM image of dsDNA with gold beads, and (c) Measured current after successive active bridging rounds, resulting in bridging.

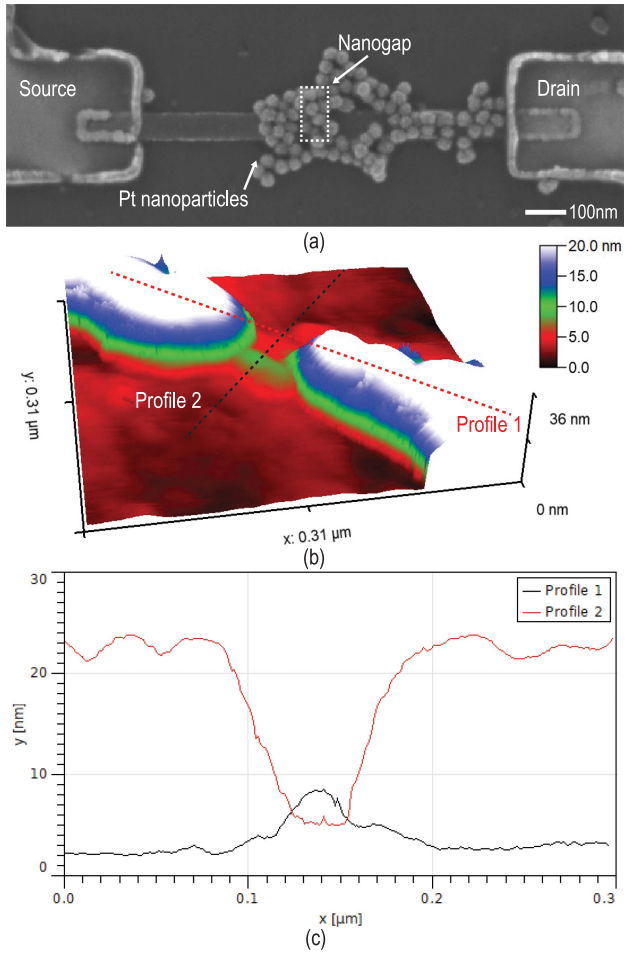

Fig. 17. (a) SEM images of platinum nanoparticles trapped between electrodes, (b) 3D AFM image of a bridge between electrodes, and (c) Profile along the annotated lines.

beads capping a 25 nm dsDNA molecular wire) spanning the electrode gap is shown in Fig. 16(b). In theory, multiple bridges could bind to a sensor. This is controlled by limiting the number of DEP rounds and observing the sensors after each round of bridging.

Orthogonal (non-electrical) verification of a single bridge molecule in the circuit is challenging due to their nanometer dimensions and low contrast. Platinum nanoparticles ($d = 30$ nm) can be trapped in the gap and easily imaged with SEM, as shown in Fig. 17(a); however, similar direct imaging of peptide or dsDNA bridges is impossible. Instead, one must either label the bridge with metal nanoparticles for SEM imaging or measure the nm changes in z-height with atomic force microscopy (AFM). Fig. 17(b) shows an AFM image of a nanoelectrode with a single bridge molecule. This process is slow and limited in the scanning area and is therefore only used for proof-of-concept verification rather than for routine systematic assessments.

To show this platform's versatility, we demonstrate a model "diagnostic" assay, specifically a protein binding or "antigen" test. The probe on the peptide bridge is a DNA aptamer (a single-stranded DNA, about 100 nt in length) having an affinity for his-tagged proteins with a reported binding affinity, K_{d}, of approximately 1-3 picomolar (pM) [45]. The target protein is the "RBD" fragment of the Spike (or S-) protein from the surface of the COVID-19 virus, produced with a histidine tag (histag). The scheme is shown in Fig. 18(a), where the aptamer is attached to the bridge using a "click" chemistry linker [13]. In the presence of the target RBD protein, the sensor current exhibits pulses corresponding to individual aptamer-protein binding events, as shown in Fig. 18(b). As expected, the rate of pulse detection (and the fraction of time in the bound state) increases with higher target molecule concentration, while the pulse widths remain constant on average as they are governed only by the binding energy of the interaction. The bound/unbound states in the signal time traces were identified by analysis with a 3-state Hidden Markov Model (HMM) [46]. In these experiments, more than 1000 binding events are analyzed from 3-minute period of target concentration exposure. Plotting the fraction of the time bound versus the target concentration, as shown in Fig. 18(c), produces a classical binding response curve of a Michaelis-Menten form. Using this, we find the aptamer has a measured disassociation constant, K_{d}, of 1.3 pM in phosphate-buffered saline (PBS) solution, in good agreement with the reported value [45]. Finally, and critically important for real diagnostic applications, we show this sensor can also work directly in physiological fluids by measuring similar target concentration response curves in pure PBS, 20% human plasma in PBS, and 100% artificial human plasma. Table I lists the fitted assay parameters, including the 95% confidence interval (CI), that are in close agreement regardless of the sample matrix and are similar to values reported in the literature for such aptamers. Critically, the sensor output is flat in the absence of the target protein and in the presence of diverse off-target molecules, indicating that the sensor is highly specific, despite being extremely sensitive.

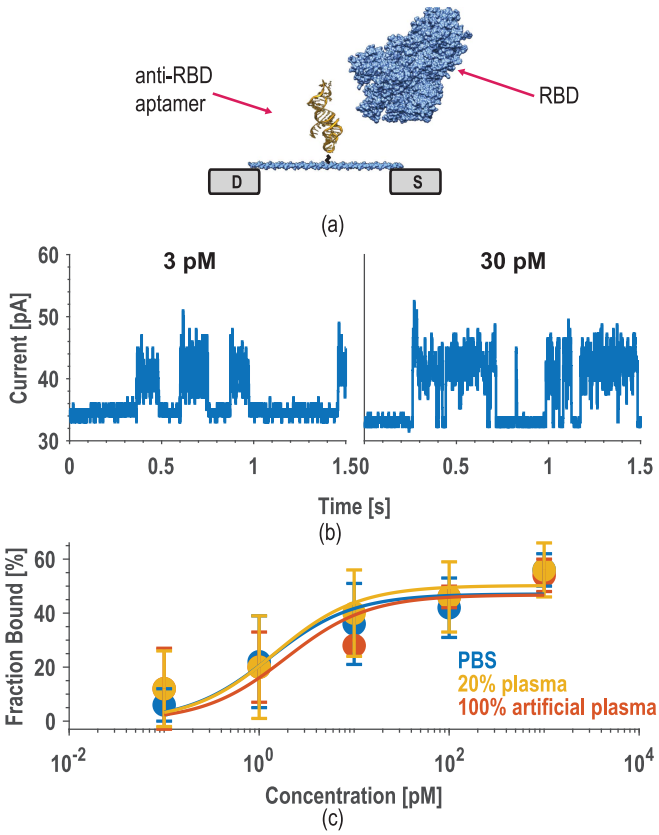

Fig. 18. (a) Scheme for COVID-19 his-tagged protein assay; (b) Current vs. time trace at different concentrations; and (c) Calibration curve showing fraction bound vs. concentration.

TABLE I
MEASURED ASSAY PARAMETERS

	PBS Buffer		20% Plasma		100% Artificial Plasma	
	Value	95% CI	Value	95% CI	Value	95% CI
B_{max}	0.47	0.4-0.55	0.47	0.39-0.58	0.5	0.41-0.6
K_d (pM)	1.3	0.4-4.5	1.9	0.39-11	1.5	0.35-5.7

This is only one of the many possible assays that this sensor device supports. We have also shown that the probe molecule can be ssDNA, antibodies, aptamers, and enzymes [13]. Of particular interest is the case where the probe is a DNA polymerase enzyme, such as Phi29. When this sensor is provided with a primed ssDNA template and free nucleotides, the polymerase can be observed in real-time to copy the template, where the specific pulses represent individual nucleotide incorporation events. This sensor provides the basis for long-read, rapid sequencing of single DNA molecules by using the pulse features to identify which pulses represent A, G, T, and C events. In this context, the extreme scalability of the CMOS molecular electronics chip offers the potential to dramatically reduce the time and cost of whole genome sequencing, which requires measuring billions of such events.

VII. CONCLUSION

This work reported the first CMOS molecular electronics chip, configured to be a programmable biosensor based on a molecular wire trapped between two nanoelectrodes of a current monitoring circuit. A 16k pixel CMOS chip was designed with a sub-pA sensitivity and 1000 frame/s readout rate to monitor probe-target molecule interactions. Post-processing techniques were developed to scalably fabricate nanoelectrodes with sub-30 nm gaps using EBL and foundry-compatible photolithography. Finally, we demonstrated the biosensor functionality with a model COVID-19 diagnostic assay performed in a complex physiological (plasma) sample.

This chip can also monitor single-molecule binding interactions for antibody-antigen and drug-receptor binding or for monitoring CRISPR/Cas enzyme activity. For such diverse biosensing applications, this platform provides the foundation for creating assays with high levels of multiplexing, rapid response on the scale of seconds, a limit-of-detection down to single molecules, and a dynamic range of pulse rate spanning many orders of magnitude. This is combined with the simplicity of label-free detection and deployment on low-cost CMOS chips and compact instruments that are well-suited to highly distributed applications. In summary, this work presents the first molecular electronics CMOS biosensor chip and demonstrates its broad utility for single-molecule sensing applications.

Competing interest statement: D.A.H., S.J., and J.M.T. are members of the Roswell Biotechnologies, Inc. Scientific Advisory Board, which entitles them to certain financial interests in the company. D.A.H. has also performed paid consulting for Roswell.

ACKNOWLEDGMENT

The authors would like to acknowledge the contributions of past and present employees of Roswell, whose collective efforts made this work possible, and Emad AlZaben, Sue Smalley, and Kevin Wall for their long-standing encouragement and support. We dedicate this work to the memory of Dr. Mark Reed, whose pioneering work, vision, and encouragement inspired many to work towards the goal of molecular electronics.

REFERENCES

[1] A. Aviram and M. A. Ratner, "Molecular rectifiers," *Chem. Phys. Lett.*, vol. 29, no. 2, pp. 277–283, Nov. 1974.
[2] G. E. Moore, *Cramming More Components Onto Integrated Circuits*. New York, NY, USA: McGraw-Hill, 1965.
[3] A. Kowalsky, "A study of the mechanism of electron transfer in cytochrome c," *J. Biol. Chem.*, vol. 244, no. 24, pp. 6619–6625, Dec. 1969, doi: 10.1016/S0021-9258(18)63451-9.
[4] R. P. Feynman, "Plenty of room at the bottom," in *Proc. APS Annu. Meeting*, 1959, pp. 1–7.
[5] M. A. Reed, C. Zhou, C. J. Muller, T. P. Burgin, and J. M. Tour, "Conductance of a molecular junction," *Science*, vol. 278, no. 5336, pp. 262–254, Oct. 1997.
[6] R. F. Service, "Molecules get wired," *Science*, vol. 294, no. 5551, pp. 2442–2443, Dec. 2001, doi: 10.1126/science.294.5551.2442.
[7] M. Bohr, "A 30 year retrospective on dennard's MOSFET scaling paper," *IEEE Solid-State Circuits Soc. News-Lett.*, vol. 12, no. 1, pp. 11–13, Nov.–Jan. 2007, doi: 10.1109/N-SSC.2007.4785534.
[8] M. Bohr, "The new era of scaling in an SoC world," in *Proc. IEEE Int. Solid-State Circuits Conf. - Dig. Tech. Papers*, 2009, pp. 23–28, doi: 10.1109/ISSCC.2009.4977293.
[9] F. Schwierz and J. J. Liou, "Status and future prospects of CMOS scaling and Moore's law—A Personal perspective," in *Proc. IEEE Latin Amer. Electron. Devices Conf.*, 2020, pp. 1–4, doi: 10.1109/LAEDC49063.2020.9073539.

[10] S. Forouhi, R. Dehghani, and E. Ghafar-Zadeh, "CMOS based capacitive sensors for life science applications: A review," *Sens. Actuators Phys.*, vol. 297, Oct. 2019, Art. no. 111531, doi: 10.1016/j.sna.2019.111531.
[11] A. Hassibi, N. Wood, and A. Manickam, "CMOS biochips: Challenges and opportunities," in *Proc. IEEE Custom Integr. Circuits Conf.*, 2018, pp. 1–7, doi: 10.1109/CICC.2018.8357043.
[12] D. A. Hall et al., "A CMOS molecular electronics chip for single-molecule biosensing," in *Proc. IEEE Int. Solid- State Circuits Conf.*, 2022, vol. 65, pp. 1–3, doi: 10.1109/ISSCC42614.2022.9731770.
[13] C. W. Fuller et al., "Molecular electronics sensors on a scalable semiconductor chip: A platform for single-molecule measurement of binding kinetics and enzyme activity," *Proc. Nat. Acad. Sci.*, vol. 119, no. 5, Feb. 2022, Art. no. e2112812119, doi: 10.1073/pnas.2112812119.
[14] P. Singh, "SPR biosensors: Historical perspectives and current challenges," *Sens. Actuators B: Chem.*, vol. 229, pp. 110–130, Jun. 2016, doi: 10.1016/j.snb.2016.01.118.
[15] Á. I. López-Lorente and B. Mizaikoff, "Mid-infrared spectroscopy for protein analysis: Potential and challenges," *Anal. Bioanalytical Chem.*, vol. 408, no. 11, pp. 2875–2889, Apr. 2016, doi: 10.1007/s00216-016-9375-5.
[16] "Beyond mass spectrometry, the next step in proteomics." Accessed: Jul. 15, 2022. [Online]. Available: https://www.science.org/doi/10.1126/sciadv.aax8978
[17] S. Alseekh et al., "Mass spectrometry-based metabolomics: A guide for annotation, quantification and best reporting practices," *Nature Methods*, vol. 18, no. 7, pp. 747–756, Jul. 2021, doi: 10.1038/s41592-021-01197-1.
[18] A. Armston, *The Immunoassay Handbook*, 4th ed. Oxford, U.K.: Elsevier, 2013. Accessed: Jul. 15, 2022. [Online]. Available: https://www.elsevier.com/books/the-immunoassay-handbook/wild/978-0-08-097037-0
[19] F. X. R. Sutandy, J. Qian, C.-S. Chen, and H. Zhu, "Overview of protein microarrays," *Curr. Protoc. Protein Sci.*, vol. 72, no. 1, pp. 27–21, Apr. 2013, doi: 10.1002/0471140864.ps2701s72.
[20] K. Shah and P. Maghsoudlou, "Enzyme-linked immunosorbent assay (ELISA): The basics," *Brit. J. Hosp. Med.*, vol. 77, no. 7, pp. C98–C101, Jul. 2016, doi: 10.12968/hmed.2016.77.7.C98.
[21] C.-L. Hsu, A. Sun, Y. Zhao, E. Aronoff-Spencer, and D. A. Hall, "A 16×20 electrochemical CMOS biosensor array with in-pixel averaging using polar modulation," in *Proc. IEEE Custom Integr. Circuits Conf.*, 2018, pp. 1–4.
[22] A. C. Sun, E. Alvarez-Fontecilla, A. G. Venkatesh, E. Aronoff-Spencer, and D. A. Hall, "High-density redox amplified coulostatic discharge-based biosensor array," *IEEE J. Solid-State Circuits*, vol. 53, no. 7, pp. 2054–2064, Jul. 2018, doi: 10.1109/JSSC.2018.2820705.
[23] H. Li, X. Liu, L. Li, X. Mu, R. Genov, and A. J. Mason, "CMOS electrochemical instrumentation for biosensor microsystems: A review," *Sensors*, vol. 17, no. 1, 2016, Art. no. 74.
[24] K. A. White, G. Mulberry, and B. N. Kim, "Parallel 1024-ch cyclic voltammetry on monolithic CMOS electrochemical detector array," *IEEE Sensors J.*, vol. 20, no. 8, pp. 4395–4402, Apr. 2020, doi: 10.1109/JSEN.2019.2961809.
[25] P. S. Singh, "From sensors to systems: CMOS-integrated electrochemical biosensors," *IEEE Access*, vol. 3, pp. 249–259, 2015, doi: 10.1109/ACCESS.2015.2410256.
[26] S.-Y. Lu et al., "A review of CMOS electrochemical readout interface designs for biomedical assays," *IEEE Sensors J.*, vol. 21, no. 11, pp. 12469–12483, Jun. 2021, doi: 10.1109/JSEN.2021.3056443.
[27] S. Hwang, C. N. LaFratta, V. Agarwal, X. Yu, D. R. Walt, and S. Sonkusale, "CMOS microelectrode array for electrochemical lab-on-a-chip applications," *IEEE Sensors J.*, vol. 9, no. 6, pp. 609–615, Jun. 2009, doi: 10.1109/JSEN.2009.2020193.
[28] X. Zhou, M. Sveiven, and D. A. Hall, "A CMOS magnetoresistive sensor front-end with mismatch-tolerance and sub-ppm sensitivity for magnetic immunoassays," *IEEE Trans. Biomed. Circuits Syst.*, vol. 13, no. 6, pp. 1254–1263, Dec. 2019, doi: 10.1109/TBCAS.2019.2949725.
[29] X. Zhou et al., "A 9.7-nT_{rms}, 704-ms magnetic biosensor front-end for detecting magneto-relaxation," *IEEE J. Solid-State Circuits*, vol. 56, no. 7, pp. 2171–2181, Jul. 2021, doi: 10.1109/JSSC.2020.3043669.
[30] D. A. Hall, R. S. Gaster, K. A. A. Makinwa, S. X. Wang, and B. Murmann, "A 256 pixel magnetoresistive biosensor microarray in 0.18 μm CMOS," *IEEE J. Solid-State Circuits*, vol. 48, no. 5, pp. 1290–1301, May 2013, doi: 10.1109/JSSC.2013.2245058.
[31] D. Ying, C.-Y. Tseng, P.-W. Chen, Y.-H. Lo, and D. A. Hall, "A 30.3 fA/Hz biosensing current front-end with 139 dB cross-scale dynamic range," *IEEE Trans. Biomed. Circuits Syst.*, vol. 15, no. 6, pp. 1368–1379, Dec. 2021, doi: 10.1109/TBCAS.2021.3124197.
[32] D. A. Hall et al., "16.1 A nanogap transducer array on 32 nm CMOS for electrochemical DNA sequencing," in *Proc. IEEE Int. Solid-State Circuits Conf.*, 2016, pp. 288–289, doi: 10.1109/ISSCC.2016.7418020.
[33] J. Musayev, Y. Adlgüzel, H. Külah, S. Eminoğlu, and T. Akln, "Label-free DNA detection using a charge sensitive CMOS microarray sensor chip," *IEEE Sensors J.*, vol. 14, no. 5, pp. 1608–1616, May 2014, doi: 10.1109/JSEN.2014.2301693.
[34] L. Keeble, N. Moser, J. Rodriguez-Manzano, and P. Georgiou, "ISFET-based sensing and electric field actuation of DNA for on-chip detection: A review," *IEEE Sensors J.*, vol. 20, no. 19, pp. 11044–11065, Oct. 2020, doi: 10.1109/JSEN.2020.2998168.
[35] A. Cornish-Bowden, "One hundred years of Michaelis–Menten kinetics," *Perspective Sci.*, vol. 4, pp. 3–9, Mar. 2015, doi: 10.1016/j.pisc.2014.12.002.
[36] Y. Choi et al., "Single-molecule lysozyme dynamics monitored by an electronic circuit," *Science*, vol. 335, no. 6066, pp. 319–324, Jan. 2012, doi: 10.1126/science.1214824.
[37] Y. Choi et al., "Dissecting single-molecule signal transduction in carbon nanotube circuits with protein engineering," *Nano Lett.,* vol. 13, no. 2, pp. 625–631, Feb. 2013, doi: 10.1021/nl304209p.
[38] T. J. Olsen et al., "Electronic measurements of single-molecule processing by DNA polymerase I (Klenow fragment)," *J. Amer. Chem. Soc.*, vol. 135, no. 21, pp. 7855–7860, May 2013.
[39] S. Sek, "Review: Peptides and proteins wired into the electrical circuits: An SPM-based approach," *Biopolymers*, vol. 100, no. 1, pp. 71–81, 2013, doi: 10.1002/bip.22148.
[40] B. Zhang, E. Ryan, X. Wang, W. Song, and S. Lindsay, "Electronic transport in molecular wires of precisely controlled length built from modular proteins," *ACS Nano*, vol. 16, no. 1, pp. 1671–1680, Jan. 2022, doi: 10.1021/acsnano.1c10830.
[41] B. Zhang, W. Song, J. Brown, R. Nemanich, and S. Lindsay, "Electronic conductance resonance in non-redox-active proteins," *J. Amer. Chem. Soc.*, vol. 142, no. 13, pp. 6432–6438, Apr. 2020, doi: 10.1021/jacs.0c01805.
[42] S. Lindsay, "Ubiquitous electron transport in non-electron transfer proteins," *Life*, vol. 10, no. 5, May 2020, Art. no. 72, doi: 10.3390/life10050072.
[43] M. A. Miled and M. Sawan, "Dielectrophoresis-based integrated lab-on-chip for nano and micro-particles manipulation and capacitive detection," *IEEE Trans. Biomed. Circuits Syst.*, vol. 6, no. 2, pp. 120–132, Apr. 2012, doi: 10.1109/TBCAS.2012.2185844.
[44] S. Sorgenfrei, C. Chiu, M. Johnston, C. Nuckolls, and K. L. Shepard, "Debye screening in single-molecule carbon nanotube field-effect sensors," *Nano Lett.*, vol. 11, no. 9, pp. 3739–3743, Sep. 2011, doi: 10.1021/nl201781q.
[45] S. Tsuji et al., "RNA aptamer binding to polyhistidine-tag," *Biochem. Biophys. Res. Commun.*, vol. 386, no. 1, pp. 227–231, Aug. 2009, doi: 10.1016/j.bbrc.2009.06.014.
[46] I. Sgouralis and S. Pressé, "An introduction to infinite HMMs for single-molecule data analysis," *Biophys. J.*, vol. 112, no. 10, pp. 2021–2029, May 2017, doi: 10.1016/j.bpj.2017.04.027.

Drew A. Hall (Senior Member, IEEE) received the B.S. degree (with Hons.) in computer engineering from the University of Nevada, Las Vegas, NV, USA, in 2005, and the M.S. and Ph.D. degrees in electrical engineering from Stanford University, Stanford, CA, USA, in 2008 and 2012, respectively. From 2011 to 2013, he was a Research Scientist with Integrated Biosensors Laboratory, Intel Corporation, Santa Clara, CA. Since 2013, he has been with the Department of Electrical and Computer Engineering, University of California San Diego, La Jolla, CA, where he is currently an Associate Professor. His research interests include bioelectronics, biosensors, analog circuit design, medical electronics, and sensor interfaces. Dr. Hall won first place in the Inaugural International IEEE Change the World Competition and first place in the BME-IDEA Invention Competition, both in 2009. He was also the recipient of the Analog Devices Outstanding Designer Award in 2011, Undergraduate Teaching Award in 2014, Hellman Fellowship Award in 2014, NSF CAREER Award in 2015, and NIH Trailblazer Award in 2019. He is also a Tau Beta Pi Fellow. He has been an Associate Editor for IEEE TRANSACTIONS ON BIOMEDICAL INTEGRATED CIRCUITS since 2015, a member of the CICC Technical Program Committee since 2017, a member of the ISSCC Technical Program Committee since 2020, and an Associate Editor for IEEE SOLID-STATE CIRCUITS LETTERS since 2021.

Nagaraj Ananthapadmanabhan received the B.E. degree in electronics and communication engineering from the College of Engineering Guindy, Anna University, Chennai, India, in 2005, and the M.S. degree in electrical engineering from Arizona State University, Tempe, AZ, USA, in 2008. From 2007 to 2012, he was an analog mixed signal circuit design Engineer with Precision Analog Division, Texas Instruments, Tucson, TX, USA. From 2012 to 2015, he was a Senior Electrical Engineer with the Power Management Group, Qualcomm Inc., San Diego, CA, USA. From 2015 to 2019, he was a Senior Electrical Engineer and the Director of Electrical Engineering with Stratos Genomics, Seattle, WA, USA. Since 2019, he has been with Roswell Biotechnologies, San Diego, as the Director of Electrical Engineering and VP of Electrical Engineering. His research interests include high-precision analog mixed signal circuits, analog and digital signal processing circuits and systems, biosensors, medical electronics, and power management.

Chulmin Choi received the Ph.D. degree in material science and engineering from the University of California San Diego, La Jolla, CA, USA, in 2010. From 2003 to 2005, he was a Research Scientist with the Samsung Advanced Institute of Technology, Suwon, South Korea. From 2012 to 2014, he was a Postdoctoral Research Fellow of the U.S. Department of Energy (DOE) Solar Program's Energy Efficiency and Renewable Energy (EERE). From 2015 to 2016, he was a Research Engineer with Oracle Labs, San Diego, CA. Since 2017, he has been employed with Roswell Biotechnologies, San Diego, as the Director of Nanofabrication. His main research interests include nanostructure design and fabrication for new energy materials related to nanostructured solar cells and bio-device for DNA sequencing

Le Zheng (Member, IEEE) received the B.S. degree in microelectronics from Fudan University, Shanghai, China, in 2007, the M.S. degree in electrical engineering from the University of California Irvine, Irvine, CA, USA, in 2009, and the Ph.D. degree in electrical engineering from the University of California Santa Cruz, Santa Cruz, CA, in 2015. From 2015 to 2016, he was a Research Engineer with Hewlett Packard Labs, Palo Alto, CA. From 2016 to 2021, he was a Principal Electrical Engineer with Roswell Biotechnologies, San Diego, CA. He is currently a Principal Electrical Engineer with Detect, Guilford, CT, USA, where he develops molecular diagnosis platforms. His research interests include bioelectronics, biosensors, and medical diagnostic systems. He is a reviewer for 14 international journals and conferences. He holds 22 U.S. patents.

Paul P. Pan received the B.S. degree (with Hons.) in electrical engineering from the University of California Santa Barbara, Santa Barbara, CA, USA, in 2006, and the M.S. degree in electrical engineering from Columbia University, New York, NY, USA, in 2010. From 2006 to 2008 and 2008 to 2010, he was a Readout IC Design Engineer with FLIR Systems Inc, Santa Barbara. Between 2012 and 2021, he worked on mixed-signal IC and system designs of various display and sensing technologies at Qualcomm, Roswell Biotechnogies, and Dexcom, all in San Diego CA. Since 2021, he has been developing sensing hardware with Apple Inc, San Diego.

Christoph Von Jutrzenka received the M.S. degree in microtechnologies from the West Saxon University of Applied Sciences of Zwickau, Zwickau, Germany, in 2008. From 2008 to 2013, he was a Mixed Signal Design Engineer with PE-Engineering, Dresden, Germany. From 2013 to 2016, he was an ASIC Architect at Bosch Sensortec, Dresden, Germany. From 2017 to 2021, he was a Senior Mixed Signal Engineer with Senseeker Engineering, Inc., Santa Barbara, CA, USA. Since 2021, he has been with Roswell Biotechnologies, San Diego, CA, as a Principal Electrical Engineer and Mechanical Prototyping Engineer. His research interests include signal processing, sensor interfaces, and rapid prototyping.

Thuan Nguyen received the B.S. degree in electrical engineering from San Diego State University, San Diego, CA, USA, in 2002. From 2008 to 2018, he was a Senior Hardware Engineer with Qualcomm Inc., San Diego. Since 2020, he has been a Senior Hardware Engineer with Roswell Biotechnologies, designing hardware for biochip bring up.

Jose Rizo received the B.Sc. degree in molecular synthesis and the M.Sc. degree in organic chemistry from the University of California San Diego, La Jolla, CA, USA, in 2018 and 2020, respectively. He is currently with Roswell, as a Senior Associate Scientist designing and employing bio-conjugation strategies to produce probes of interest. His research interests include medicinal chemistry, pharmacology, synthetic chemistry, and organometallic chemistry. Aside from research, he is deeply passionate about community outreach and empowering the next generation of scientists.

Macklan Weinstein received the B.S. degree in mathematics from the University of San Diego, San Diego, CA, USA, in 2016, and the master's degree in mathematics from Claremont Graduate University, Claremont, CA, in 2018. From 2018 to 2019, he was an Algorithm Engineer with Edwards Lifesciences, Irvine, CA. Since 2019, he has been a Principal Signal Processing Engineer with Roswell Biotechnologies, San Diego.

Raymond Lobaton received the B.S. degree in chemistry and materials science from University of California, Los Angeles, CA, USA in 2019. From 2018 to 2020, he was a Process Engineer with NanoClear Technologies, Pasadena, CA. At NanoClear, he worked on optoelectronic device fabrication and developed novel methods for surface energy modification of glass and plastic substrates. Since 2020, he has been a Nanofabrication Engineer with Roswell Biotechnologies, San Diego, CA.

Prem Sinha received the M.Sc. degree in biotechnology from Madurai Kamaraj University, Madurai, India, in 2002, and the Ph.D. degree in biochemistry from the University of Bielefeld, Bielefeld, Germany, in 2007. From 2007 to 2012, he was a Research Associate with Scripps Research Institute, San Diego, CA, USA, where he researched mitochondrial complex I. From 2012 to 2015, he did research in osmolyte biophysics area as a Research Associate with Pennsylvania State, Hershey, PA, USA. From 2015 to 2016, he worked with BASF Enzymes, San Diego, on enzyme engineering and evolution. As a Senior Staff Scientist with Molecular Assemblies, San Diego, from 2017 to 2019, he worked toward developing an enzymatic DNA synthesis platform. Since November 2019, he has been with Roswell Biotechnologies, San Diego, where he is leading protein engineering and assay development efforts. His research interests include biochemistry, biosensors, biophysics, enzyme evolution, assay development, and DNA sequencing.

Trevor Sauerbrey received the B.A. degree in interdisciplinary computing in the arts and media from the University of California San Diego, La Jolla, CA, USA, He is currently working toward the Master of Applied Data Science from the University of San Diego, San Diego, CA. While completing the B.A. degree, he was a Research Assistant with Dorris Neuroscience Center, The Scripps Research Institute, La Jolla. Since 2019, he has been working with Roswell Biotechnologies as a Data Scientist on the Signal Processing Team and responsible for the data analysis of single molecule binding assays and DNA sequencing.

Cruz Sigala will receive the B.S. degree in molecular and cellular biology from the University of San Diego, San Diego, CA, USA, in 2023. Since May 2022, he has been a Research Associate with Roswell Biotechnologies, San Diego, assisting in assay development and biosensor engineering.

Kathryne Bailey received the B.S. degree (with Hons.) in biological sciences from Manchester Metropolitan University, Manchester, U.K., in 1997, and the Ph.D. degree in environmental microbiology from Warwick University, Coventry, U.K., in 2006. From 2006 to 2011, she conducted postdoctoral research into microbial anaerobic oxidation pathways with UC Berkeley, CA, USA. From 2019 to 2021, she developed a novel lateral flow type detection device for an anti-counterfeit ink system with Diversified Nano Inc, Poway, CA. Since 2021, she has been the Director of Assay Development, pushing the boundaries of single molecule detection.

Paul J. Mudondo received the B.S. degree in geomatic/survey engineering from the University of Nairobi, Nairobi, Kenya, in 1993, and the M.Sc. degree in financial engineering from London Metropolitan Business School, London, U.K. He joined Roswell as a Principal Software Engineering Lead in late 2019 as an experienced leader in software development and commercial cloud deployment infrastructure. He has 25 years of commercial expertise in software development, Big Data processing, machine learning development, and deployment on hybrid environments. He led multiple global digital transformations and financial trading platform development programs at various investment banks, including HSBC, Goldman Sachs, JP Morgan, and UBS.

Ashesh Ray Chaudhuri received the M.S. degree in microelectronics from the Indian Institute of Technology Kharagpur, Kharagpur, India, in 2010. He joined the Ph.D. Program at the University of Catholic de Louvain, Brussels, Belgium, in collaboration with IMEC, Belgium. In 2014, he joined the team of process integration engineers at IMEC, focusing on microelectromechanical systems (MEMS) sensors. In 2012, he joined Life Science Technology Department, IMEC and started to focus on fabricating sensors for medical applications. In 2018, he was appointed as a Team Leader of process technology responsible for fabricating sensors for DNA sequencing. In 2020, he became the Principal Member of Technical Staff at IMEC, focusing on early research and development of sensors for various applications. He has more than 10 years of semiconductor fabrication experience working in advanced manufacturing facilities. He holds several peer-reviewed papers and granted patents.

Simone Severi received the M.Sc. degree from the University of Bologna, Bologna, Italy, in 2001, and the Ph.D. degree from the Katholieke Universiteit Leuven, Leuven, Belgium, in collaboration with IMEC, Belgium, in 2006. In 2007, he joined IMEC, focusing on the process integration of microelectromechanical systems (MEMS), and in 2009 appointed as MEMS Team Leader. In 2012, he joined Life Science Technology Department, IMEC and started to focus his attention on biosensors and ufluidic devices for medical applications. In 2020, he was the Department Director, process technology responsible for life science, MEMS specialty sensors, and GaN power electronics. He is currently the Life Sciences Program Director. He has authored or coauthored more than 100 papers and has 10 granted patents.

Carl W. Fuller received the B.A. degree (*cum laude*) in honors biochemistry and the Ph.D. degree from the University of Pennsylvania, Philadelphia, PA, USA, in 1974 and 1979, respectively.. From 1980 to 1984, he did postdoctoral investigation with Harvard University, Cambridge, MA, USA, with Charles C. Richardson, focusing on the replication of Bacteriophage T7.

From 1984 to 1993, he was a Senior Scientist with United States Biochemical Corp., Cleveland, OH, USA, focused on DNA polymerases for Sanger DNA Sequencing and PCR. From 1992 to 1993, he did further work on primers and polymerases for sequencing with Brookhaven National Laboratory, Upton, NY, USA, as a Visiting Scientist. From 1993 to 1999, he was with Amersham Pharmacia Biosciences, and moved to Piscataway, NJ, USA, in 1999, as the Science Director. In 2004, G.E. Healthcare acquired the company, and he became VP, Science Fellow, where he remained till 2009. During 2010–2011, he worked with Life Technologies, Beverly, MA, and Foster City, CA, USA. During 2012–2014, he was with Single-Molecule Nanopore Sequencing Startup Genia when it was acquired by Roche 2014–2017. During 2017–2019, he was with Singular Genomics, La Jolla, CA. Since 2019, he has been with Roswell Biotechnologies, San Diego, CA, working on single-molecule electronic sensors for DNA sequencing and other applications. He was the recipient of the 1977 National Research Service Award, 1981 ACS Fellowship, and 1993 Enterprise Development Innovation Award. From 1994-1996, he was the Study Section Chair of American Heart Association. His other activities include 2015–2020, DNA sequencing study section NIH-NHGRI and 2006–2008 Grant "Closed Complex Single Molecule Sequencing."

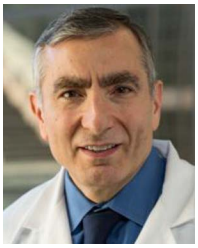

James M. Tour received the Bachelor of Science degree in chemistry from Syracuse University, Syracuse, NY, USA, and the Ph.D. degree in synthetic organic and organometallic chemistry from Purdue University, West Lafayette, IN, USA. He did Postdoctoral training in synthetic organic chemistry with the University of Wisconsin, Madison, WI, USA, and Stanford University, Stanford, CA, USA. After spending 11 years with the Faculty of the Department of Chemistry and Biochemistry, University of South Carolina, Columbia, SC, USA, he joined the Center for Nanoscale Science and Technology , Rice University, Houston, TX, USA, in 1999, where he is currently the T. T. and W. F. Chao Professor of chemistry, Professor of computer Science, and Professor of materials science and nanoengineering. He is also a Synthetic Organic Chemist. He has more than 750 research publications, more than 130 granted patents, and more than 100 pending patents. He has an h-index = 165 with total citations more than 125 000. In 2021, he won the Oesper Award from the American Chemical Society, which is awarded to "outstanding chemists for lifetime significant accomplishments in the field of chemistry with long-lasting impact on the chemical sciences." In 2020, he became a Fellow of the Royal Society of Chemistry and, in the same year, was awarded the Royal Society of Chemistry's Centenary Prize for innovations in materials chemistry with applications in medicine and nanotechnology. He was inducted into the National Academy of Inventors in 2015. He was named among "the 50 most influential Scientists in the world today" by TheBestSchools.org in 2019; listed in "the world's most influential scientific minds" by Thomson Reuters.

Sungho Jin received the B.S. degree in metallurgical engineering from Seoul National University, Seoul, South Korea, in 1969, and the M.S. and Ph.D. degrees in materials science and engineering from the University of California, Berkeley, CA, USA, in 1971 and 1974, respectively. After joining Bell Labs, Murray Hill, NJ, USA, in 1976, he carried out forefront materials and devices research for 26 years. He then joined the University of California San Diego, San Diego, CA, in 2002 as a Distinguished Professor and Iwama Endowed Chair, and was the Director of the University-Wide Materials Science and Engineering Program for 13 years. He retired from the University of California San Diego in 2015 as Professor Emeritus. He is currently a Consulting Scientist and Senior Advisor for Roswell Biotechnologies, San Diego. His research interests and activities include nanomaterials, energy materials, magnetic materials, and biomaterials. Dr. Jin is a member of the U.S. National Academy of Engineering (1999), U.S. National Academy of Inventors (2017), Fellow of American Physical Society, Fellow of American Society for Metals, TMS Fellow, and MRS Fellow. He was the Journal Editor of *Acta Materialia* (2007–2021). He was the recipient of various awards/recognitions, including the John Bardeen Award in 2007, Ho-Am Engineering Prize in 2000, Albert-Sauveur Achievement Award in 2009, CRS Jorge Heller JCR Award in 2012, and Acta Gold Medal in 2016.

Paul W. Mola received the post-graduation degree in biotechnology and business. He is currently the Chief Executive Officer and President of Roswell Biotechnologies, Inc., and a member of the company's board of directors. A significant portion of his career has been focused on deploying biology on semiconductor chips. In his role as the Head of Strategy and Chief of Staff of the Genetic Systems Division of Life Technologies, he played a critical role in bringing to market the first semiconductor sequencing technology. He founded Roswell in 2014 to realize the promise of the Molecular Electronics chip. He is a member of the board of governors of Biocom, the San Diego State Mission Valley Innovation District Advisory Group, and the Fleet Science Center Board of Trustees.

Barry Merriman received the B.S. degree in mathematics and the second B.S. degree in physics from The University of Washington, Seattle, WA, USA, and the Ph.D. degree in applied mathematics from the University of Chicago, Chicago, IL, USA. He was on the Faculty of University of California, Los Angles (UCLA), Los Angles, CA, USA, for 20 years, from 1989 to 2009, where he led research programs spanning math, computer science, physics, nuclear fusion engineering, human genetics, and genomics. In industry, from 2009 to 2014, he was with Life Technologies (now a division of Thermo Fisher Scientific) as a Lead Architect for advanced DNA sequencing technology, where his program led the development of the ion torrent ISFET CMOS chip sequencing device, and the Genia nanopore CMOS chip sequencing device. He was also the Chief Science Officer of the Enterprise Genomics Solutions Business Unit, which supported national-scale genomics projects worldwide, including the Saudi Human Genome Project in the Kingdom of Saudi Arabia and The Million Veterans Program in the USA. He was also the VP of Global Technology Assessment with Human Longevity Inc. from 2014 to 2016, developing precision medicine for cancer therapy with genomics pioneer Dr. Craig Venter. Since 2016, he has been the Co-Founder and CSO of Roswell Biotechnologies. He has authored or coauthored more than 100 papers, with more than 22 000 citations, an h-index of 52, and he has 35 granted patents. Dr. Merriman was an NSF Postdoctoral Fellow of Mathematics, The Johnson Scholar in Genetics with UCLA. At Life Technologies he was the recipient of Game Changer Award, their highest honor for work that transforms the company. He was selected for the Early Entrance Program at the University of Washington, where he was admitted to the University at age 14.